

A Peculiar Linear Radio Feature In The Supernova Remnant N206

Robert J. Klinger, John R. Dickel, Brian D. Fields

Astronomy Department, University Of Illinois at Urbana-Champaign, Urbana, IL 61801

and

Douglas K. Milne

Australia Telescope National Facility, Epping NSW 1710, Australia

Received _____; accepted _____

ABSTRACT

We present images of the supernova remnant N206 in the LMC, taken with ATCA at wavelengths of 3 and 6 cm. Based on our data and previously published flux densities, the spectral index of N206 is -0.20 ± 0.07 . The 6-cm radio morphology shows a filled center. Most interesting is the discovery of a peculiar linear feature previously undetected at any wavelength. The feature lies to the east of the center of the remnant, stretching from about one-fourth to three-fourths of the remnant's radius. It is wedge-shaped, with a steady opening angle from an apex on the eastern side. The feature resembles the disturbance expected from an object moving through the material supersonically at about 800 km/s. We present arguments suggesting that the linear feature might have been produced by a low-mass star or compact object ejected from a binary system which may have led to a Type Ic supernova.

Subject headings: ISM: Supernova Remnants, Radiation Mechanisms: Nonthermal, Radio Continuum: ISM, Stars: Pulsars: General, Polarization

1. Introduction

Several studies of supernova remnants (SNRs) in the Large Magellanic Cloud (LMC) have included the SNR located on the north-eastern edge of the H II region LH α 120-N206 (Henize 1956). In following common practice, we will henceforth use the name N206 for the SNR or use its coordinate designation B0532-710.

Radio observations were made at several frequencies, ranging from 0.4 to 14.7 GHz (Mathewson & Clarke 1973; Milne, Caswell, & Haynes 1980; Milne et al 1984) with resolutions on the order of a few arcminutes. The data showed a bright source with a

relatively flat radio spectrum with an index of about -0.33 (Milne, Caswell, & Haynes 1980). However, the observations were complicated by the presence of the nearby H II region to the south-west of the SNR and were unable to resolve any structure in the interior of the remnant.

H α images of N206 show a roughly circular filamentary shell around the periphery (Williams et al 1999). Images taken in [S II] and [O III] (Lasker 1977) also show a shell structure with little central emission. When combined with the earlier radio data, the optical images indicate that the object could be considered a shell type SNR.

X-ray data have been obtained with both Einstein and *ROSAT*. These images show a centrally brightened morphology with no apparent edge brightening to denote an X-ray shell (Long, Hellfand, & Grabelsky 1981; Williams et al 1999). By X-ray morphology alone, the remnant is classified as centrally-brightened. However, when combined with the radio and optical morphology, the remnant has been suggested to be of the class called “mixed morphology” (Rho & Petre 1998), due to the disparity between the observed morphologies when viewed at different wavelengths. The centrally concentrated X-ray emission from mixed morphology remnants is thermal. Currently available X-ray data are insufficient to determine whether or not the emission is thermal.

In this paper, we present high resolution (Half-Power Beam Widths (HPBW) 1.1" and 1.8") radio images of N206 at 3 and 6 cm made with the Australia Telescope Compact Array (ATCA). These images show no detailed structure in the remnant except for a linear feature that was previously undetected at radio wavelengths and is also absent from both optical and X-ray images of the SNR.

The observations and data reduction are discussed in Section 2 of this paper. Radio images and descriptions of the radio morphology, spectral information, and polarization measurements are presented in Section 3. A discussion of the observed features is in Section

4. Conclusions are in Section 5.

2. Observations

We observed N206 with the Australia Telescope Compact Array (ATCA). Data were taken on five observing nights in late 1997. The observing parameters and observing dates are given in Table 1. The baselines were distributed between 31 m and 6 km, giving good coverage throughout that region of the spatial frequency plane. The observations were made at 4798 and 8638 MHz with bandwidths of 100 MHz in polarization mode, giving data on all four Stokes parameters.

For each observation, the flux calibrator source PKS B1934-638 was observed at the beginning and end of the run. The phase calibrator chosen was the point source, PKS B0454-810 for the first four data sets and PKS B0530-727 for the fifth data set. In all observations, the phase calibrator was observed at approximately 20 minute intervals to allow for proper phase correction. Flux densities for the calibrators are given in Table 1.

Data reduction was carried out with the *MIRIAD* package (Sault, Teuben, & Wright 1995). The data were calibrated and formed into dirty images before cleaning and restoring with circular beams. The circular HPBW sizes were 1.1" and 1.8" for the 3-cm and 6-cm images respectively. The images were made with ROBUST weighting (Briggs 1995) to maintain high angular resolution but provide as much sensitivity as possible.

Polarization maps were also made with the *MIRIAD* package. Dirty images were made in Stokes Q , U , and I , cleaned, and restored using the circular beams mentioned above. To reduce the noise level, each image was convolved with a 5" beam. The *MIRIAD* task IMPOL was then used to combine the convolved maps in the different Stokes parameters to make a polarized intensity map and a position angle map. These maps were used to

determine the strength and direction of the magnetic field. The *MIRIAD* task IMRM was used to calculate the Faraday rotation measure across the SNR.

3. Results

3.1. Morphology

3.1.1. Overall SNR

The final radio images at 6 and 3 cm are shown in Figures 1a and 1b, respectively. The supernova remnant is $180 \text{ arcseconds} \times 195 \text{ arcseconds}$ in size, slightly elongated in roughly the east-west direction. Throughout the paper, we will adopt a distance to the LMC of 50 kpc (Feast 1999). Using this, we find a linear size for the remnant of 44 pc by 47 pc (north-south and east-west respectively). At 6 cm, the remnant has diffuse emission across its entire face. The eastern side is twice as bright as the western edge, with a steady gradient showing decreasing emission from east to west. This brightness gradient can be seen in the one dimensional slices through the 6-cm image shown in Figure 2. Although the east-west slices may indicate the presence of a shell, they still show that the central emission from the remnant stays well above the background. Based solely on this morphology, the remnant may be classified as a filled or Crab-like or perhaps a composite remnant.

The structure of the SNR is less obvious in the 3-cm image. The morphology of the remnant from this image may indicate edge-brightening on the north-eastern and south-western edges, similar to what is seen at 6 cm. Unfortunately, because of the smaller beamwidth, the surface brightness of the remnant at 3 cm is significantly lower than at 6 cm. The peak brightness of the map is just over the $3\text{-}\sigma$ ($\sigma_{3\text{cm}} = 3.4 \times 10^{-5} \text{ Jy beam}^{-1}$) noise level, in contrast to over $6\text{-}\sigma$ ($\sigma_{6\text{cm}} = 6.0 \times 10^{-5} \text{ Jy beam}^{-1}$) for the 6-cm image. The fainter emission is lost in the noise in the 3-cm image. Natural weighting was tried to

increase sensitivity to the large-scale emission, but it also emphasized the side lobes and did not significantly improve the image quality. Therefore, nothing can be said about the morphology of the remnant’s interior at 3 cm.

Figures 3a and 3b show *ROSAT* HRI (Williams 1999) and H α (Magellanic Clouds Emission Line Survey; Smith 1999) images of N206, overlaid with 6-cm radio contours. The *ROSAT* HRI image shows a somewhat elliptical central brightening with a gradual and isotropic decrease in brightness with increasing radial distance from the remnant’s center. There is no apparent brightening on the eastern or western edges. In contrast, the radio image does not show strong emission from the remnant’s center; the brightest region is in the eastern half of the remnant.

The H α image shows a very filamentary structure and a distinct shell to the remnant. These filaments and shell are also prominent in images taken in [S II] and [O III] (Lasker 1977).

Although the optical emission is primarily in filaments, there is some diffuse optical emission in the center of the remnant in the H α image. As seen in echelle data, this central emission represents a stationary component (attributed to emission from the nearby H II region), whereas the emission from the expanding SNR has a velocity of around 250 km s⁻¹ (Chu & Kennicutt 1988). To further test the nature of this central emission, we interpolated between the integrated radio and X-ray flux densities. We found that the estimated flux density from synchrotron emission in the optical is several orders of magnitude too low to appear in the H α image. Therefore, this diffuse optical emission does indeed seem to arise from the nearby H II region rather than from optical synchrotron emission from the SNR.

3.1.2. Peculiar Linear Feature

In the eastern side of the remnant is a linear feature, oriented east-west and stretching from a point roughly 25 arcseconds west of the center of the remnant. This feature is approximately 55 arcseconds (13 pc) in length, ending approximately 20 arcseconds from the eastern edge of the SNR. The widest point of this feature is at its western end, narrowing steadily toward the east with a Full-Width at Half Maximum (FWHM) of less than 5 arcseconds at its eastern tip. Included in Figure 2 are two 1-D slices through the 6-cm data (slices 4 and 5). Once Gaussian profiles are fitted to each slice, the FWHM of the feature can be determined, along with the error of the fit. The results of this process are given in Figure 4, showing the FWHM of the linear feature as a function of distance from the remnant’s center.

This linear feature has never been detected before at any wavelength. Although the optical image shows that the remnant has a filamentary structure, there are no filaments that appear associated with the linear feature in the radio image. The X-ray image shows that the brightest emission is concentrated in the remnant’s center and appears to be reasonably spherically distributed. In addition, there is no point source located at either end of the feature in any of the wavelength bands. The origin of this linear structure is not known, but will be further examined below (§ 4).

While some other SNRs exhibit long thin features, they can be seen as parts of shell filaments visible in both radio and optical images. One structure that may be similar to what we see in N206 is a linear feature in G84.2–0.8, but that also has a point radio source at one end (Matthews and Shaver 1980). To our knowledge, the linear feature in N206 is the first such feature seen in an SNR without accompanying filamentary structure or a point source.

3.2. Spectral Index

Using the ATCA data, we obtained flux densities of 0.52 ± 0.07 Jy at 4798 MHz and 0.49 ± 0.12 Jy at 8638 MHz. There is a gradient in the background level due to contamination from the H II region located to the south-west of the remnant. Taking a mean value for the background led to the above flux density measurements. Although no integrated flux density measurements in the literature cite errors (with the exception of that by Mills et al 1984 who give an expected error of around 10%), we believe that our error at 6 cm should be comparable with the other measurements.

All flux density values available for N206 are listed in Table 2 and the spectrum of the remnant is shown in Figure 5. The flux density scale for all the given values, except the 843 MHz MOST result (Mills et al. 1984) has been checked and is found to agree with the current ATNF scale based on the calibration source PKS B1934-638 (Reynolds 1994). The calibration scale used for the MOST during the early commissioning phase when the measurement was made is somewhat uncertain but should be within 5% of the current one. A linear, unweighted regression to the data (i.e. a power law fit) with a slope of -0.20 ± 0.07 is also plotted. Such a value is typical for a spectral index expected from a filled center SNR ($S \sim \nu^\alpha$, $-0.4 < \alpha < 0$) but is flatter than is generally found for a shell-type remnant ($-0.8 < \alpha < -0.3$) (Trushkin 2000).

The faintness of the 3 cm data makes it difficult to make a spectral index map of the remnant. To try to increase the sensitivity, both the 3-cm and 6-cm images were convolved with $5''$ circular beams. The convolved images were both masked at the $1-\sigma$ level and the spectral index map shown in Figure 6 was made. Although the 3-cm image still suffers from low sensitivity, the resulting map does give reasonable results for the linear feature since the signal to noise ratio is considerably better in this region than in the rest of the remnant. In the vicinity of the linear feature, the spectral index is approximately -0.2 , in

good agreement with the results for the entire SNR from the previous figure.

3.3. Polarization

The polarization map of the region around the linear feature in N206 is shown in Figure 7. The vector length represents the 6-cm polarized intensity and the vector direction is that of the intrinsic *magnetic* field after correcting for the Faraday rotation. For this image, the polarized intensity at both wavelengths was greater than 1.5σ . Although most of the vectors are associated with the peculiar linear feature, this is a brightness effect. The fractional polarization on the linear feature was approximately 15%. Unfortunately, the signal-to-noise ratio on the remainder of the remnant was insufficient to reliably determine the magnetic field direction or the fractional polarization, although it does appear that there is some polarization throughout the SNR.

The rotation measure determined from the position angle rotation between 6 and 3 cm is about $+200$ radians/m², increasing slightly as you move from west to east along the linear feature. After correcting for the Faraday rotation, we find that the magnetic field at the location of the linear feature is aligned nearly along the feature. It seems likely that this direction is representative of the field in the feature itself and not of the remnant as a whole. However, without knowledge of the global magnetic field orientation in the SNR, we cannot be certain of this assessment.

Even more interesting is the hint of a twisting of the magnetic field near the center of the linear feature. This can be seen as a change in the direction of the vectors in Figure 7 where the magnetic field vectors are oriented roughly north-west to south-east. There is also a variation in the polarized intensity at this location in the center of the jet in the figure shown. This spot has brighter emission in the total radio intensity and approximately

zero rotation measure. This leads us to believe that there could be some thermal emission at this spot from a dense clump with a field alignment which adds some negative Faraday rotation to bring the mean closer to zero. The material in the linear feature is apparently clumpy.

4. Discussion

4.1. Classification of the Remnant

The classification of this SNR is not straight forward. The radio emission is nearly uniform with a smooth brightness gradient from east to west across the face of the remnant (Fig. 2). The X-ray emission is centrally peaked while the optical spectral lines indicate a shell structure. We await XMM-Newton spectra to see if the X-ray emission is thermal or non-thermal. The radio spectral index of -0.20 is typical of a Crab-like SNR and is lower than the value expected for a shell-type remnant (Trushkin 1999). It may be a composite remnant in which the plerion component has reached the shell or the shell may just be forming. In either case, we suggest that there is at least a component to the SNR that may be powered by an unseen pulsar. The lack of a detectable pulsar is true for several other Crab-like SNRs, e.g. 3C58 (Bocchino et al. 2001), G21.5-0.9 (Slane et al. 2000), and G328.4+0.2 (Gaensler, Dickel, & Green 2000).

The more rapid decay in X-ray brightness toward the edges of the remnant may be explained by the fact that the X-ray synchrotron emission would decay faster, leaving primarily radio synchrotron emission in the outer regions. A pulsar could still be bright in thermal X-rays, due to its high temperature, but available X-ray observations have insufficient spatial resolution to detect a possible X-ray point source in the SNR. The observed X-ray emission may be partly thermal as well. Additional observations are needed

at higher spectral and spatial resolution.

If the remnant is indeed Crab-like, at 47 pc in diameter, it is the largest one known, almost twice the size of the previously largest known Crab-type remnant G328.4+0.2 (Gaensler, Dickel, & Green 2000). Following the method of Gaensler, Dickel, & Green to relate the pulsar spindown energy to the expansion of the surrounding wind nebula, we can estimate the age of the remnant based on the size of the apparent plerion. By taking the wind as a pressure source driving the swept-up material, one can relate the nebular age to its size, the energy injection rate, and the ambient density. Since a distinct separate radio shell is not observed, we will take the size of the plerion to be the entire measured size of the remnant, 23.5 parsecs in radius. Using the spectrum given above, we obtain a radio luminosity (L_r) for the remnant of 9.25×10^{34} erg s⁻¹ when we integrate from 100 MHz to 100 GHz. We define $\epsilon = L_r/\dot{E} \sim (1 - 5) \times 10^{-4}$ (Gaensler et al. 2000) for Crab-type remnants, where \dot{E} is the pulsar energy loss rate. We will adopt the mean value, $\epsilon = 3 \times 10^{-4}$. Taking the initial ISM particle density prior to the supernova event of 0.003 cm⁻³, we obtain an age of 29,000 years for the remnant. As we would expect, N206 is probably the oldest of the Crab-like remnants.

This age is, of course, only a very rough estimate. For example, the density used may be an underestimate, especially considering the presence of an H II region southwest of the remnant. However, increasing the density would only lead to an increased estimate for the age.

4.2. Peculiar Linear Feature

The linear feature seen in both the 3 and 6-cm images is unusual. It is bright and present in both the 3 and 6-cm images, and it is not associated with any filaments in the

remnant. The data used to create the maps shown in Figures 1a and 1b were taken on five separate observing nights, spaced over a three month time period and when maps were made from each individual data set, the linear feature appeared in every one. Thus, it is extremely unlikely that it could be an instrumental problem. Our conclusion is that it is a real feature that requires explanation.

One question that needs to be addressed is whether the feature is actually associated with the remnant or is the result of a line of sight coincidence. Recall that the data indicate a shallow spectral index for the feature, similar to the spectral index for the whole remnant. If the linear feature were a jet, as from a radio galaxy along the line of sight, one would expect to find a much steeper spectral index (e.g. Jarvis et al 2001). Also, if a radio galaxy were responsible for the linear feature, we might expect the galaxy itself to appear in the images. There is no evidence for a point or extended source at either end of the linear feature in either the radio or the optical images. In addition, the linear feature is aligned radially with the center of the remnant. Such a chance alignment is unlikely unless the feature is physically associated with the SNR.

We conclude that this linear feature is most likely to be physically associated with the remnant. If indeed this is true, the mechanism by which this emission is created must be energetic enough to account for the observed radio emission while low enough in energy to not produce detectable optical or X-ray emission. Other key constraints are: the lack of a point source anywhere along the linear feature, the centrally-concentrated nature of the emission at all wavelengths, and the wedge-like morphology of the linear feature.

4.2.1. Constraints on the Physical Origin of the Linear Feature

We have considered several possible mechanisms that might give rise to the linear feature, and find that the available data powerfully constrain these scenarios. For example, a key constraint arises from the spectral index information and the filled radio morphology, which lead us to classify the remnant as Crab-like. The synchrotron emission from Crab-like remnants is powered at least in part by a pulsar, although the pulsar is often not detected. Thus, any explanation of the remnant should include a pulsar. Moreover, the central X-rays and the filled-center radio morphology seem to require that the pulsar remains near the center of the remnant.

The data thus drive us to explain the linear feature in a model with a centrally located pulsar. The first possibility is that the feature is a radio jet from the central pulsar. There are two major problems with this notion. First, the feature is widest near the center and is very narrow at its farthest end (cf Figure 4), the opposite of what would be expected from a jet emanating from a central pulsar. Also, the feature appears to start at approximately 6 parsecs (25 arcseconds) from the center of the remnant, which is unlikely for a jet created by a pulsar that originated in the center of the SNR. If it is indeed a jet, it must be rather energetic to be bright out to approximately 13 parsecs away from the emitting source. Such a bright emitting source aligned in the plane of the sky should have an equally bright jet on the opposite side; such emission is not observed. If the jet is not aligned in the plane of the sky, the opposite jet may not be visible due to Doppler beaming; yet there might still be emission from any material that interacts with the relativistic particles in the jet, which is not observed. It is also unlikely that the relativistic expansion of material needed for Doppler beaming would exist that far from the emitting source. In addition, any inclination to the plane of the sky would mean that the size of the jet is greater than 13 parsecs, and thus it would have to be more energetic. The more energetic the feature, the more likely it

would be to appear in optical and X-ray bands.

Another alternative to account for the enhanced synchrotron emission is shock excitation. A shock wave can create a density enhancement in the remnant’s material. This density enhancement will also cause an enhancement in the magnetic field as the field lines are compressed. The shape of the linear feature supports the notion that it was created by an object moving supersonically through the ambient interior of the SNR and creating shock waves. Figure 4 shows that there is a correlation between the FWHM of the linear feature and its distance from the remnant’s center. If indeed the object originated in the center and moved toward the edge of the remnant at greater than the sound speed, we would expect to see a feature with this shape.

From the opening angle of the feature, we can determine the Mach number at which the object is travelling and compare the resulting length and time scales with the estimated lifetime stated previously. If this is a bow shock (due to motion in the plane of the sky), then the Mach number, M , is $M = [\sin(\theta/2)]^{-1}$, where θ is the full opening angle. From a linear regression, $\theta = 0.222 \pm 0.013$ radians, giving a Mach number of 9.0 ± 0.5 . If we use $\sim 10^6$ K as a representative temperature for the remnant, this leads to a spatial velocity for the moving object of around 800 km/s. (If the jet is inclined to the plane of the sky, the Mach number and velocity increase by roughly a factor of $(\sin i)^{-1}$, where i is the inclination angle measured relative to the line of sight.) The eastern edge of the feature is 80 arcseconds from the remnant’s center, corresponding to a linear distance of 19.4 pc. This leads to an age of 23,000 years for the remnant if the object originated in the center and maintained a nearly constant velocity. Given the uncertainties, this estimate is consistent with that found above for the SNR expansion.

Since there is consistency between the shape and the likely dynamical age for the feature, we proceed by speculating what type of object was responsible for its creation. If

a pulsar is not responsible for creating the linear feature, then from the arguments made above, the most likely candidate is a companion star. From the nearly circular shape of the remnant, we make the assumption that the explosion site was very near the geometrical center of the radio emission. The inferred companion velocity of 800 km/s places strong constraints on the binary system. Since the kick velocity of the pulsar must be small, the companion velocity must be due to its orbital motion. But in this case, the separation between the stars is very close: $a \sim 3R_{\odot} (M_1/10 M_{\odot})$, and thus we demand a very tight binary system. To avoid tidal destruction of the stars requires that they be relatively dense, with a massive primary having $\rho \gtrsim 5 \text{ g/cm}^3$, which is far higher than in a normal supergiant. We are thus forced to require that the pre-supernova be in a dense form of a bare helium (or CO) core, and thus we also demand a relatively dense companion – either a low-mass main sequence star or a compact object.

In fact, Nomoto et al. (1994) have proposed an evolutionary path that would lead to such systems and suggest that these might be the progenitors of Type Ic supernovae. Nomoto et al. estimate that the frequency of such events is about $\sim 9\%$ the rate of Type II events. Thus, while these systems would be rare, they would not be inordinately so. Consequently, we speculate that N206 could be the remnant of a binary system that led to a Type Ic supernova, with a low-mass main sequence or compact companion (white dwarf or neutron star) that has led to the peculiar linear feature.

While this model is able to explain the X-ray and radio morphologies, it is unfortunately not yet adequate to reproduce all of the observational results. The passage of the star will produce shock waves analogous to those in a shell-type supernova remnant, in which the shock waves will propagate through the surrounding material, causing compression of that material and increased synchrotron emission. Typically, the brightest emission is expected from the shock front. Thus we would expect the production of a conical structure whose

point is located at the position of the moving star. The propagating shock wave marks the outer surface of the cone. Since the cone would have a relatively evacuated center and a density enhancement behind the shock, we would expect to see an edge-brightened morphology, as in a shell-type supernova remnant. However, the brightest part of the linear feature is along the central line of the feature rather than at the edge of the wedge shape (center-brightened rather than edge-brightened). Possibly the interaction of the moving star with the supernova remnant’s material causes a large portion of the particles to become trapped at or near the center of the conical feature, rather than being carried along by the shock front, or the particles are allowed to diffuse back into the center of the cone. Perhaps the non-uniform magnetic field pattern and possible clumping found from the polarimetry data above can help to diffuse the particles back into the center of the linear feature, creating the center-brightening. This line of reasoning requires further study.

5. Conclusions

We present high-resolution ATCA images of the LMC supernova remnant N206 at 3 and 6-cm wavelengths. The remnant is roughly circular and centrally brightened in the radio, with a possible radio shell. Observations at X-ray wavelengths show a centrally-filled morphology. The optical observations show bright filaments around the edges, forming a full optical shell.

We found integrated flux densities of 0.52 and 0.49 Jy at 6 and 3-cm respectively. These values are consistent with previous radio measurements. Overall, the radio data indicate a spectral index -0.20 ± 0.07 for the remnant, typical of a Crab-type SNR.

Most peculiar to this SNR is the detection of a narrow linear feature seen in radio but undetected at other wavelengths. The feature has a roughly constant opening angle of 12

degrees, stretching from inside of the eastern edge of the remnant and becoming lost in the noise near 25 arcseconds from the center of the remnant. Taking 50 kpc as the distance to the LMC, the feature is 13 parsecs in length.

The first polarimetric maps were made for the remnant. We found linear polarization on the linear feature, the only region bright enough for reliable measurements. The polarized intensity was roughly 15% over the linear feature where the signal to noise ratio was larger than $3\text{-}\sigma$. The magnetic field seems to be aligned along the feature with a twist in the center. The polarimetry map is only reliable in the vicinity of the linear feature so a magnetic field map for the entire remnant could not be made.

From the observational data, we were able to place several constraints on our proposed model for the linear feature. From the center-filled radio morphology and spectrum, we conclude that a pulsar should exist in the SNR. Since bright X-ray emission is generally associated with a pulsar, the pulsar is not likely to be located at either end of the linear feature where little X-ray emission is detected. Rather, the X-ray emission near the center of the remnant led us to choose a model which had the pulsar spatially coincident with the strongest X-ray emission.

To satisfy the above constraints, our proposed model to explain the presence of the linear feature is the passage of a low-mass stellar object through the remnant's material at approximately Mach 9.0, which corresponds to 800 km/s for a medium at 10^6 K. The resulting shock waves produce density and magnetic field enhancement behind the object, causing the enhanced synchrotron emission. From the lack of X-ray emission associated with the feature, we speculate that the object responsible is a low-mass companion star to the supernova progenitor that was ejected from the tight binary system at the time of the explosion. Such a scenario has been proposed for Type Ic supernovae. This model is still insufficient to properly explain all of the observations, particularly the lack of limb

brightening in the wedge-shaped feature.

Better constraints on the proposed model can be made when higher resolution X-ray images and X-ray spectra become available for the remnant. The discovery of a pulsar in the remnant may clarify the situation and should help to constrain the model discussed above.

We would like to thank Miroslav Filipovic for contributing the fifth data set for our images. We would also like to thank Rosa Williams and Chris Smith for providing the Rosat and H α images. Thanks also to Ronak Shah for help with gaussian fitting and error analysis, to Martin Guerrero for help with determination of the feasibility of optical detection, and to Ron Webbink for enlightening discussions on binary systems. Finally, we are grateful to the anonymous referee for comments that led us to improve the paper. JRD was supported, in part, by the Campus Honors Program at UIUC, and the work of BDF was supported by the National Science Foundation under Grant AST-0092939.

REFERENCES

- Bocchino, F., Warwick, R. S., Marty, P., Lumb, D., Becker, W., & Pigot, C. 2001, *A&A*, 369, 1078
- Briggs, D. S. 1995, *High Fidelity Deconvolution of Moderately Resolved Radio Sources*, Ph. D. thesis, New Mexico Inst. of Mining & Technology
- Burrows, A. & Hayes, J. 1996, *Physical Review Letters*, 76, 352
- Chu, Y.-H., & Kennicutt, R. C. 1988, *AJ*, 95, 1111
- Clarke, J. N., Little, A. G., & Mills, B. Y., 1976, *Aust. J. Phys. Astrophys. Suppl.*, No. 40
- Feast, M. 1999, *PASP*, 111, 775
- Gaensler, B. M., Dickel, J. R., & Green, A. J. 2000, *ApJ*, 542, 380
- Gotthelf, E. V. & Wang, Q. D. 2000, *ApJ*, 532, L117
- Henize, K. G. 1956, *ApJS*, 2, 315
- Jarvis, M. J., Rawlings, S., Eales, S., Blundell, K. M., Bunker, A. J., Croft, S., McLure R. J., & Willott, C. J. 2001, *MNRAS*, 326, 1585.
- Lasker, B. M. 1977, *PASP*, 89, 474
- Long, K. S., Helfand, D. J., Grabelsky, D. A. 1981, *ApJ*, 248, 925
- Matthews, H. E. & Shaver, P. A. 1980, *A&A*, 85, 55
- Mathewson, D. S. & Clarke, J. N. 1973, *ApJ*, 180, 725
- Mills, D. S., Turtle, A. J., Little, A. G., Durdin, J. M. 1984, *Australian Journal of Physics*, 37, 321

- Milne, D. K., Caswell, J. L., & Haynes, R. F. 1980, MNRAS, 191, 469
- Nomoto, K., et al. 1994, Nature, 371, 227
- Reynolds, J.E. 1994, AT Doc. Ser. No. AT/39.3/040, Australia Telescope National Facility
- Rho, J. & Petre, R. 1998, ApJ, 503, L167
- Sault, R. J., Teuben, P. J., & Wright, M. C. H. 1995, Astronomical Data Analysis Software and Systems IV, ASP Conference Series, 77, 433
- Slane, P., Chen, Y., Schulz, N. S., Seward, F. D., Hughes, J. P., Gaensler, B. M. 2000, ApJ, 533, L29
- Smith, R. C. & The MCELS Team 1999, in IAU Symp. 190, New Views of the Magellanic Clouds, ed. Y.-H. Chu, J. Hesser, & N. Suntzeff (San Francisco: ASP), 28
- Strom, R. G. & Stappers, B. W. 2000 in IAU Colloquium 177, Pulsar Astronomy - 2000 and Beyond, ed. Kramer, M., Wex, N., & Wielebinski, N., (San Francisco: ASP), 509
- Trushkin, S. 1999, http://cats.sao.ru/snr_spectra.html
- Wang, Q. D. & Gotthelf, E. V. 1998, ApJ, 494, 623
- Williams, R. M., Chu, Y.-H., Dickel, J. R., Petre, R., Smith, R. C., Tavarez, M. 1999, ApJS, 123, 467

Table 1. Observing Parameters and Calibrator Flux Densities ($S_\nu =$ Flux Density)

| Date | Configuration | Calibrator | 3-cm S_ν (Jy) | 6-cm S_ν (Jy) |
|--------------|---------------|------------|-------------------|-------------------|
| Aug. 7, 1997 | 750B | 0454-810 | 1.657 | 1.092 |
| Aug. 27,1997 | 1.5C | 0454-810 | 2.030 | 1.266 |
| Oct. 10,1997 | 375 | 0530-727 | 0.265 | 0.25 |
| Oct. 23,1997 | 750C | 0454-810 | 2.509 | 1.744 |
| Nov. 11,1997 | 6C | 0454-810 | 2.393 | 1.829 |
| All | All | 1934-638 | 2.84 | 5.83 |

Table 2. Flux Densities of SNR N206

| Frequency (MHz) | S_ν (Jy) | Quoted Uncertainty | Source of Plotted Uncertainty | Reference for S_ν |
|--------------------|-----------------|-----------------------|---|-----------------------------|
| 408 | 0.7 | none given | background removal estimates by others | Matthewson & Clarke 1973 |
| 843 | 0.591 | 10% | rms noise | Mills et al. 1984 |
| 4798 | 0.52 | ± 0.07 | background subtraction | this paper |
| 8638 | 0.49 | ± 0.12 | background subtraction | this paper |
| 14700 | 0.27 | ± 0.22 | background subtraction for peak | Milne et al. 1980 |

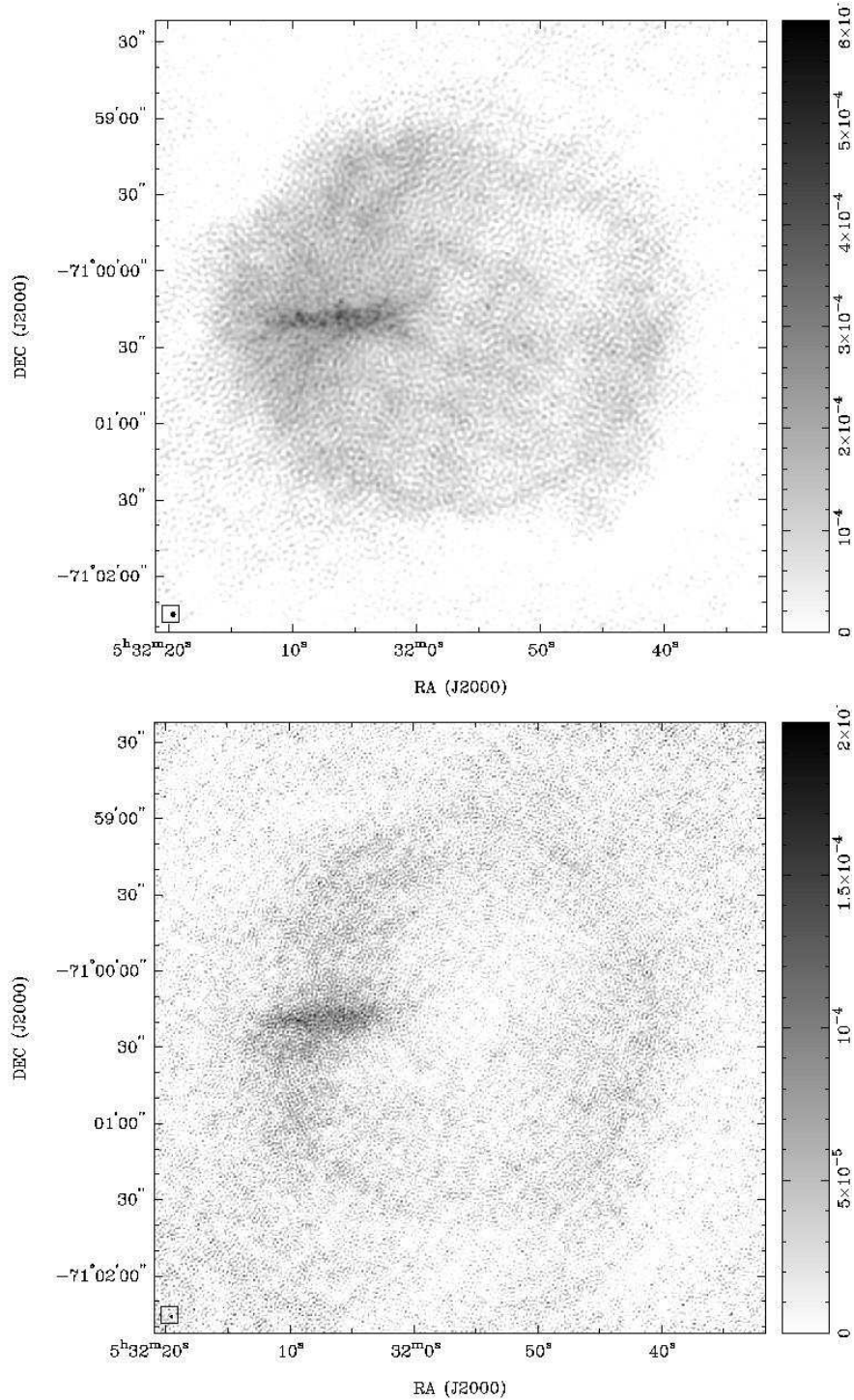


Fig. 1.— 6-cm (upper panel) and 3-cm (lower panel) radio images of the SNR N206. The units on the wedges are Jy beam^{-1} . Circular beams were used with beamwidths of $1.8''$ and $1.1''$ for the 6-cm and 3-cm images, respectively. Beam sizes are given in the lower left-hand corner of each image.

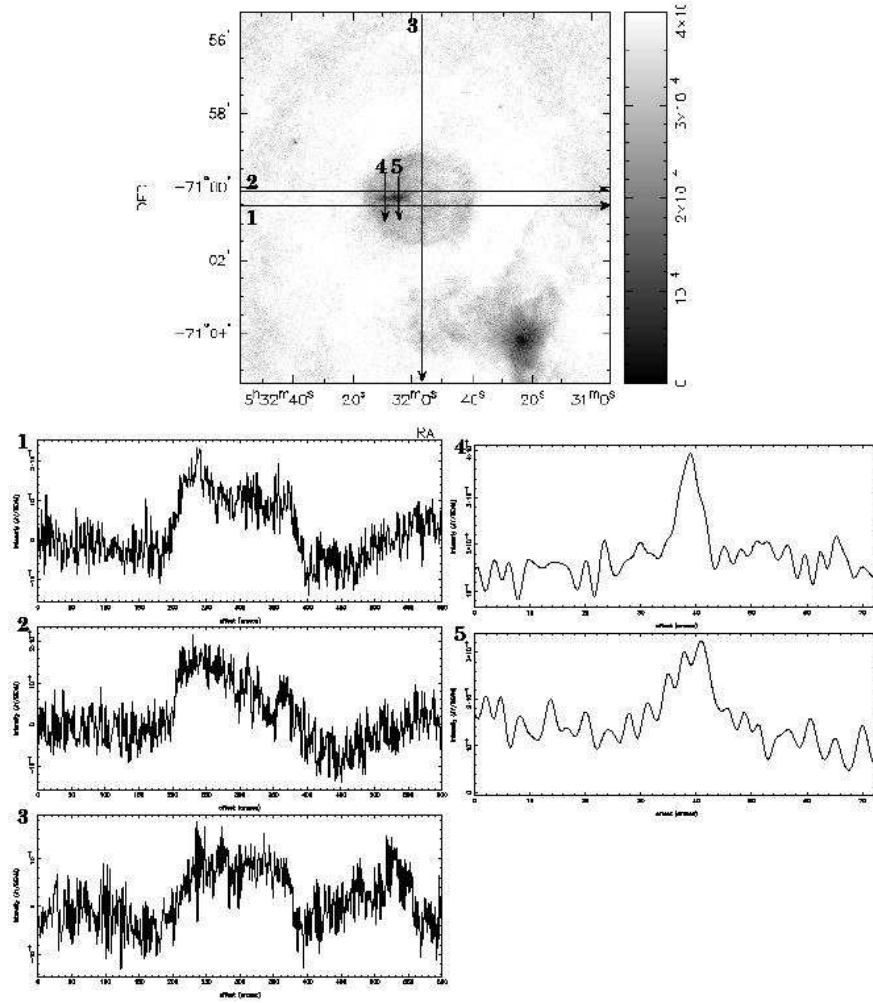


Fig. 2.— 1-dimensional slices through the 6-cm image. The bright feature at the lower right in the 6-cm image is the H II region part of N206.

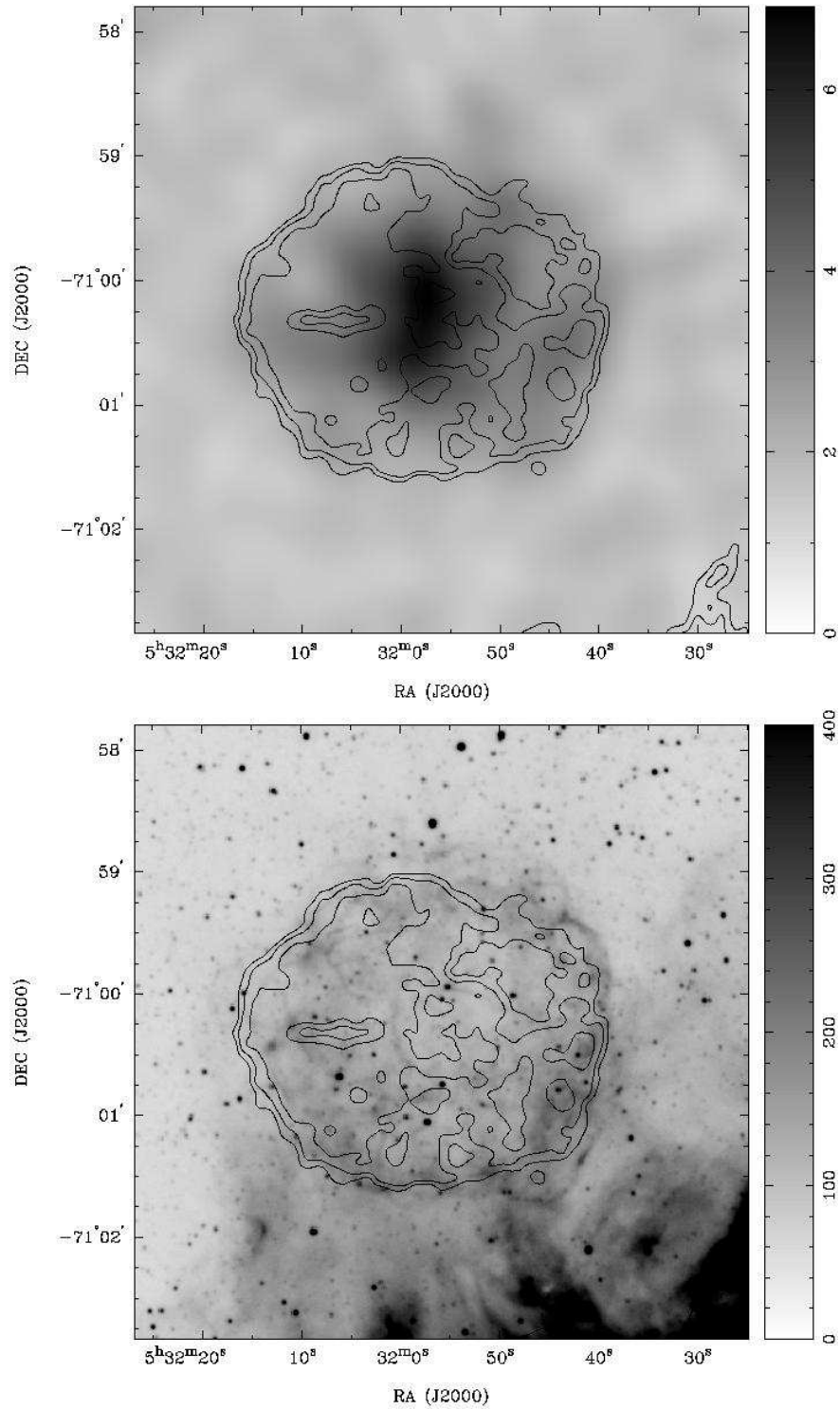


Fig. 3.— *ROSATHRI* (upper panel) and H α (lower panel) images with 6-cm radio contours. The grayscales in the upper and lower figures show the X-ray and optical counts, respectively. The contours shown in both images are 90, 75, 50, 35, and 25% of the peak radio intensity.

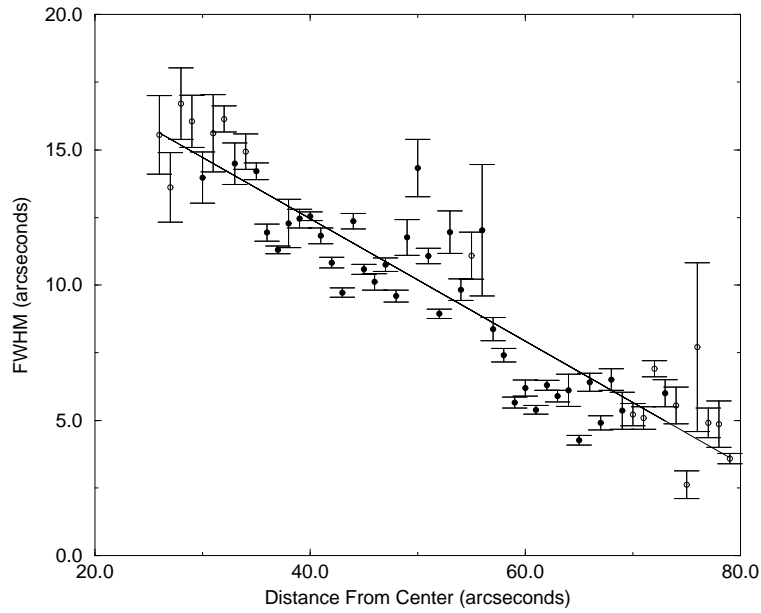


Fig. 4.— FWHM of the linear feature as a function of distance from the center: The regression slope = -0.226 ± 0.013 and the opening angle, $\theta = 12.7^\circ$. The error bars represent uncertainty in the individual Gaussian fits to the 1-D slice data taken across the linear feature. Closed circles denote slices where the peak intensity of the slice was greater than 3σ above the brightness of the surrounding remnant. Open circles represent slices for which the peak intensity of the slice was between 2 and 3σ above the brightness of the surrounding remnant.

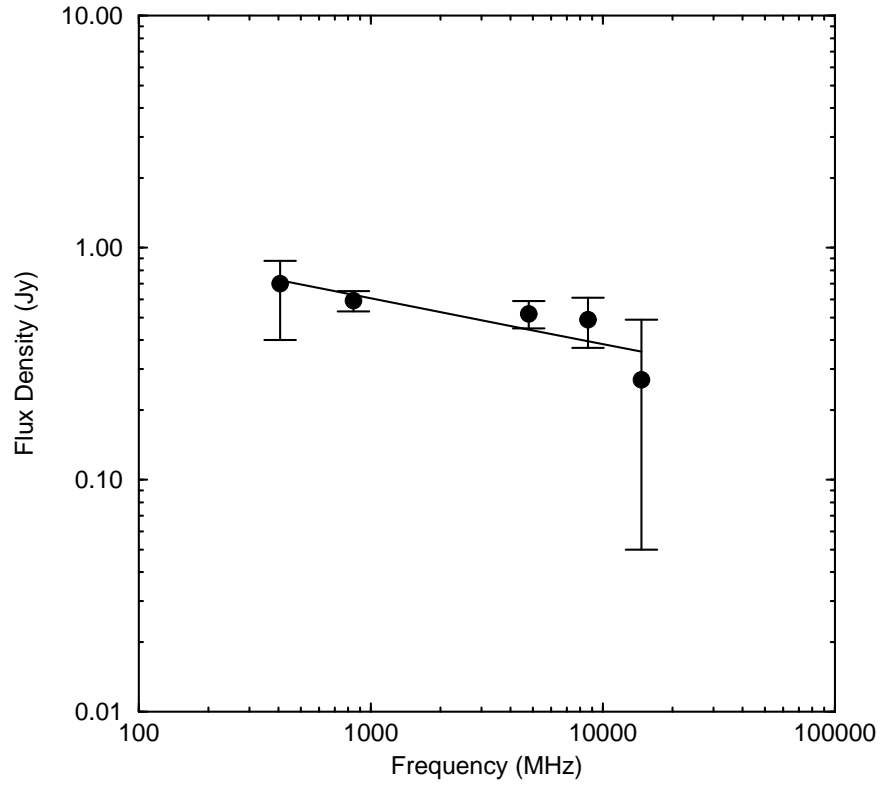


Fig. 5.— Radio spectrum of the SNR N206. Flux density values and error estimates are given in Table 2.

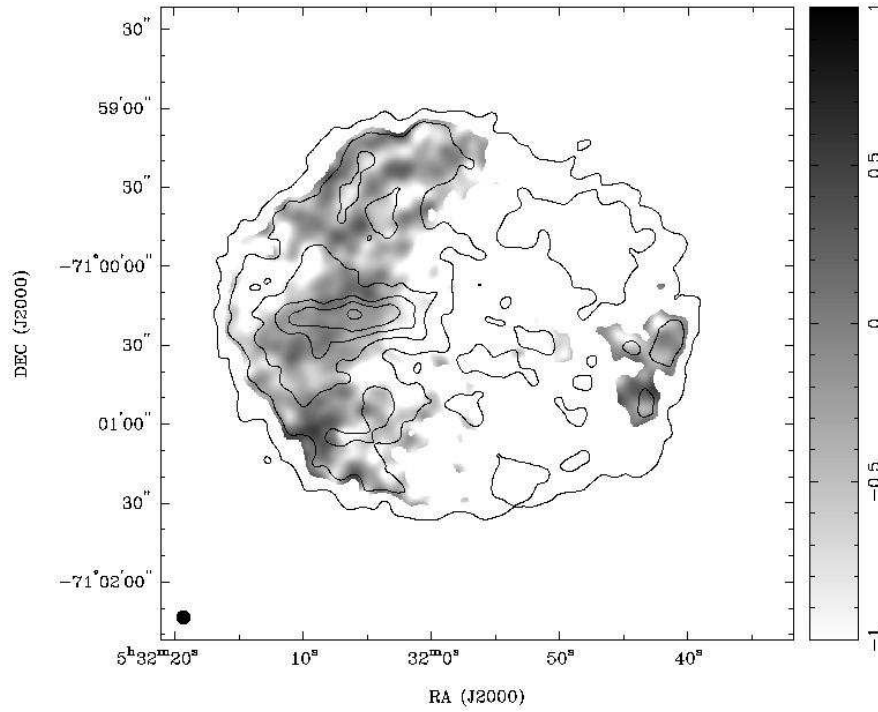


Fig. 6.— Spectral index map of the SNR N206. The grayscale denotes the spectral index across the remnant made from 3 and 6-cm images convolved to 5^{''}. The contours denote 6-cm total intensity at 95, 75, 60, 45, 30, and 15 percent of the peak intensity (5.694×10^{-4} Jy beam⁻¹). The 6-cm total intensity was also convolved to 5^{''}. The beam size is shown in the lower left.

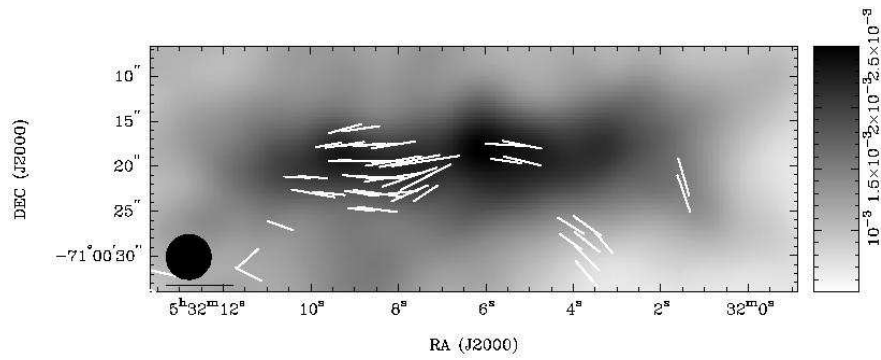


Fig. 7.— Polarization Map of the Linear Feature in N206 at 6 cm: The lengths of the vectors are scaled to the 6-cm polarized intensity. The longest vector corresponds to a polarized surface brightness of 6×10^{-5} Jy beam $^{-1}$, the length denoted by the bar at the lower left. The orientation of the vectors denotes the direction of the magnetic field. The grayscale shows the total intensity in Jy beam $^{-1}$. The beams were convolved to 5". The beam width is shown in the lower left corner.